Power-capture assessment of a nearshore, modular, flap-type wave energy converter in regular, head-on waves*

L. Wilkinson (corresponding author)[a,b], T. J. T. Whittaker[b], P. R. Thies[c], S. Day[d], D. Ingram[e]

[a]Industrial Doctoral Centre for Offshore Renewable Energy (IDCORE),
United Kingdom
l.wilkinson@ed.ac.uk

[b]Marine Research Group, School of Natural and Built Environment,
Architecture, Civil Engineering and Planning, David Keir Building, Stranmillis Road,
Queen's University Belfast, Belfast, BT9 5AG, United Kingdom
t.whittaker@qub.ac.uk

[c]College of Engineering, Mathematics and Physical Sciences,
University of Exeter, Penryn Campus, Penryn,
Cornwall, TR10 9FE, United Kingdom
p.r.thies@exeter.ac.uk

[d]Naval Architecture and Marine Engineering,
University of Strathclyde, Henry Dyer Building,
100 Montrose St, Glasgow, G4 0LZ, United Kingdom
sandy.day@strath.ac.uk

[e]Institute for Energy Systems, The University of Edinburgh,
Faraday Building, King's Buildings, Colin Maclaurin Road,
Edinburgh, EH9 3DW, United Kingdom
david.ingram@ed.ac.uk

*Manuscript of published paper: Wilkinson, L., Ocean Engineering (2017),
http://dx.doi.org/10.1016/j.oceaneng.2017.04.016

Abstract

Bottom-hinged, flap-type wave energy converters (WECs) are efficient devices, in terms of power capture, and are usually sited in the nearshore region. They typically comprise a single flap spanning their full width. However, a potentially beneficial design change would be to split the flap into multiple, vertical modules, to make a 'Modular Flap'. This could provide improvements, such as increased power production in directional waves, reduced foundation loads and lower manufacturing and installation costs. Assessed in this fundamental work is the hydrodynamic power-capture of this device, based on 30th scale physical modelling. Comparisons are made to a single, equivalent width 'Rigid Flap'. Tests are conducted in regular, head-on waves. The simplest control strategy, of damping each module equally, is employed.

The results show significant differences in the magnitudes of the power produced by individual flap modules. On average, the central modules generate 72% of the total power. Phase differences are also present. This total power produced by the Modular Flap was 28% more smooth than that generated by the Rigid Flap.

The Modular Flap had a 3.3% +/-2.9% lower power-capture than the Rigid Flap. The advantages of the modular concept may therefore be exploited without significantly compromising the power-capture of the flap-type WEC.

Keywords: wave energy converter power modular flap

1.

Introduction

There is a need to improve the economic viability of wave energy converters (WECs), in order for them to compete in the energy market. Design solutions must be found that have high energy yields, whilst offering manageable manufacturing, installation, maintenance and decommissioning costs.

Bottom-hinged flap-type WECs, also known as Oscillating Wave Surge Converters, are designed to absorb energy from the horizontal acceleration of water in ocean waves (Whittaker and Folley, 2012). They usually consist of a buoyant flap, with its hinge mounted on the seabed

(Folley et al., 2007). These devices are typically sited in the nearshore region, in water depths of 10-20 m. There is an extensive body of work on this type of device (Henry, 2008; Renzi et al., 2014; van ’t Hoff, 2009). Through comparative assessments, it has been shown to be one of the most efficient in terms of power conversion (Babarit, 2015; Babarit et al., 2012). As a result, the device type has received significant commercial focus, with a number of large scale devices deployed, such as Aquamarine Power Ltd’s Oyster machines (Henry et al., 2010; Whittaker and Folley, 2012) and AW-Energy’s WaveRoller (AW-Energy, 2012).

Most flap-type devices employ a single body for their rotating section (Folley et al., 2007). If this is large, for example 26 m in width like the Oyster 800 device (Aquamarine Power Ltd, 2011), then asymmetric pressure across the flap results in twisting of the structure, including its foundation (Wilkinson et al., 2014). The use of a single wide unit like this can also necessitate the use of large, expensive installation vessels (Aquamarine Power Ltd, 2009). Additionally, the power produced by the device is sensitive to the direction of the incident wave (Henry, 2008). A new concept, the ‘Modular Flap’, formed by splitting the rotating body into a number of narrow, mechanically independent, vertical modules, may reduce the magnitudes of these problems. This could provide improvements, such as increased power production in directional waves, reduced foundation loads, an indicator of capital cost, and lower manufacturing and installation costs. There could also be operational advantages such as increased redundancy in the system, reducing the effect of failure on one module versus a whole flap. Additionally, a modular formation would make the scaling up of devices, in terms of overall width, arguably more feasible.

There are a number of studies on offshore structures comprised of multiple flaps (Mei et al., 1994; Wilkinson et al., 2014). In Wilkinson et al (2014), it was shown that the foundation loads were reduced for such a device, by up to 73% in the parasitic twisting yaw and roll degrees of freedom. However, the application of such a device for the purpose of wave energy extraction has only recently received attention (Abadie, 2016; Sammarco et al., 2013; Sarkar et al., 2016; Wilkinson et al., 2015). These studies investigated the behaviour of the device, in terms of motion amplitudes, and most of them included a power-capture assessment. The latter is a key element of a techno-economic evaluation of a WEC concept. Sarkar et al (2016), for example, presents a mathematical power-capture assessment of a 24 m wide device, made up of six

cylindrical modules. Regular, head-on waves were used in the study. It was found that the power-capture of the modular system was highly dependent on the power take-off (PTO) damping strategy. With each module damped equally, both devices achieved similar levels of power-capture. However, using different damping on each module, the modular flap outperformed the rigid flap, due to the occurrence of multiple resonances. While this study provided an insight into the potential of the device, there were limitations of the modelling that was used, such as not considering nonlinear and viscous effects (Sarkar et al., 2016). The use of scale physical modelling can address these issues by working in a real fluid. It also provides reasonably fast generation of sufficiently long data time-series, compared to, for example computational fluid dynamics (Abadie, 2016). In this paper, physical modelling in a wave tank is used to assess the hydrodynamic power-capture of the Modular Flap. This is carried out across a range of wave conditions. Comparisons are made to a single device with an equivalent total width, referred to throughout this work as the 'Rigid Flap'. Shown first, in section 2, are the modelling and analysis methodologies, followed by presentation of the results in section 3, discussion of the significance of the results in section 4 and finally, in section 5, some conclusions and suggestions for further work.

2. Methodology

2.1

This section presents the key information on the physical modelling methodology. This includes details on the physical model, the wave conditions, the wave tank and the modelling and analysis procedures that were used. The physical modelling was conducted at 30th scale. Froude scaling has been used to convert the variables and results into full-scale values.

Physical Model

A physical model was used to represent the device in this study. The model was made up of six box-shaped, surface-piercing modules. The total width of the model was approximately 33 m at

full scale, which is similar to the Oyster 800 machine (Aquamarine Power Ltd, 2011). A single model was used to complete the tests, which could be configured either as the Modular Flap or the Rigid Flap. The Rigid Flap was formed by attaching the modules together with PVC sheets on the front and back faces. The modules, when independent, also had PVC sheets attached to them, to maintain consistent mass and geometric properties. The flap modules were mounted on a base structure, attached to the wave tank floor. 3D CAD renderings of the Modular and Rigid Flaps are provided in Figure 1; the key dimensions of the model are shown in Figure 2; the model, installed and operating in the wave tank, is shown in Figure 3; a diagram illustrating the module numbering system that is used for results presentation is shown in Figure 4.

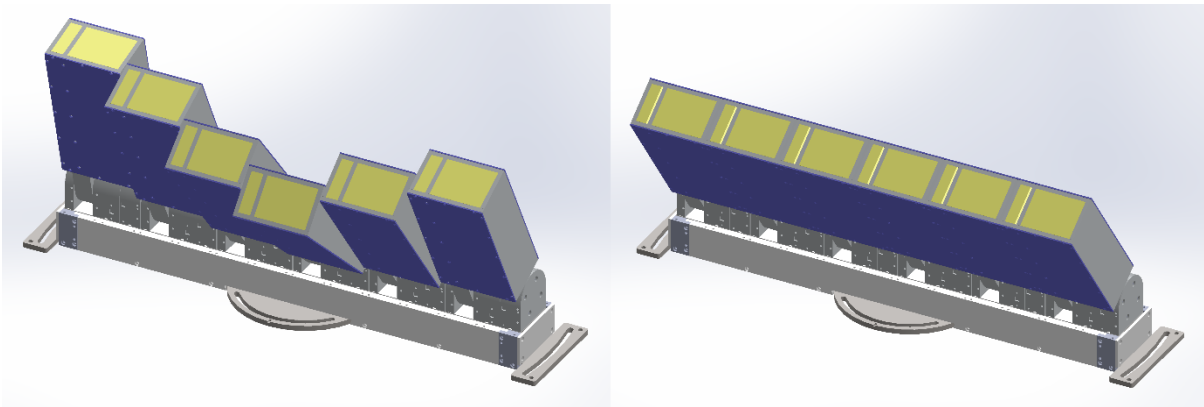

Figure 1. CAD renderings of physical model in Modular Flap (left) and Rigid Flap (right) configurations.

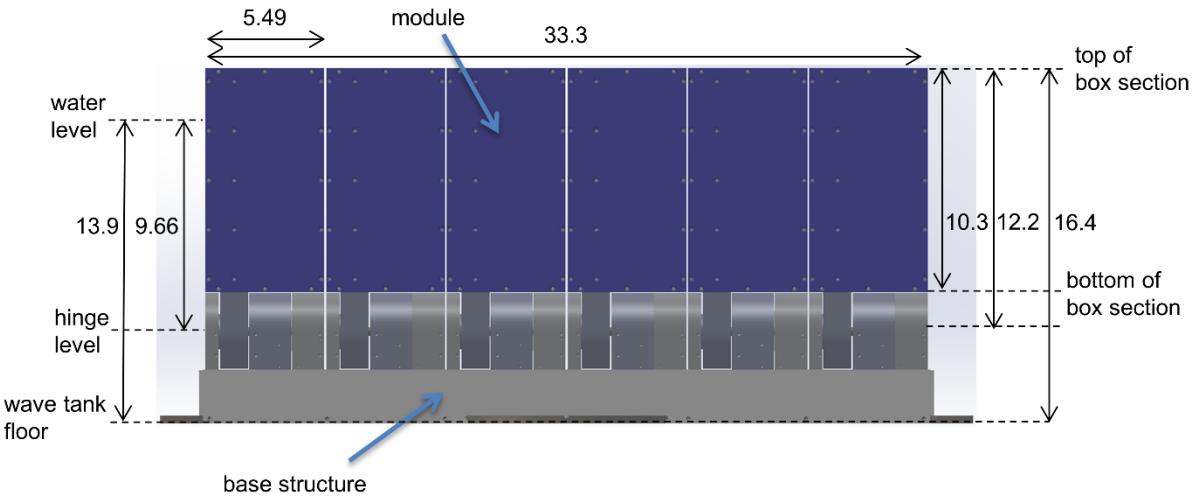

Figure 2. Device dimensions, in full scale, in m. Note that the thickness of the device was 3.6 m.

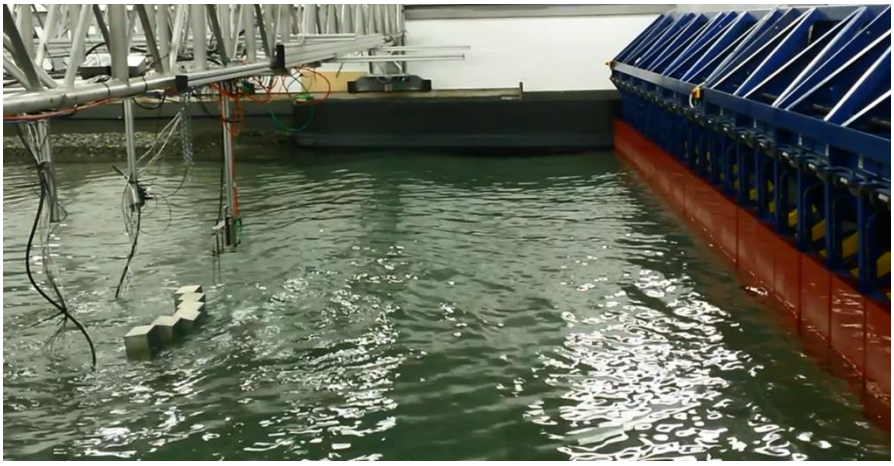

Figure 3. Photograph of the physical model, in its Modular Flap configuration, operating in the wave tank.

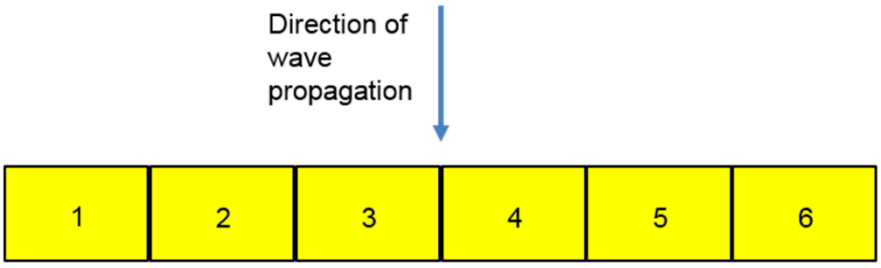

Figure 4. Plan-view diagram illustrating module numbering system. Geometry is to scale.

At the hinge axis of each module were housings for bearings and instrumentation. The instrumentation included sensors to measure instantaneous rotation and applied damping torque. Each module also contained a magnetic particle brake, to simulate a Coulomb-damping PTO mechanism. Further model details can be found in (Wilkinson et al., 2015). In this study, the simplest control strategy, of applying damping equally to each module, was applied. This was executed by controlling the supply voltages in a LabVIEW program (National Instruments, 2016). Example time-series of damping torques are shown in Figure 5.

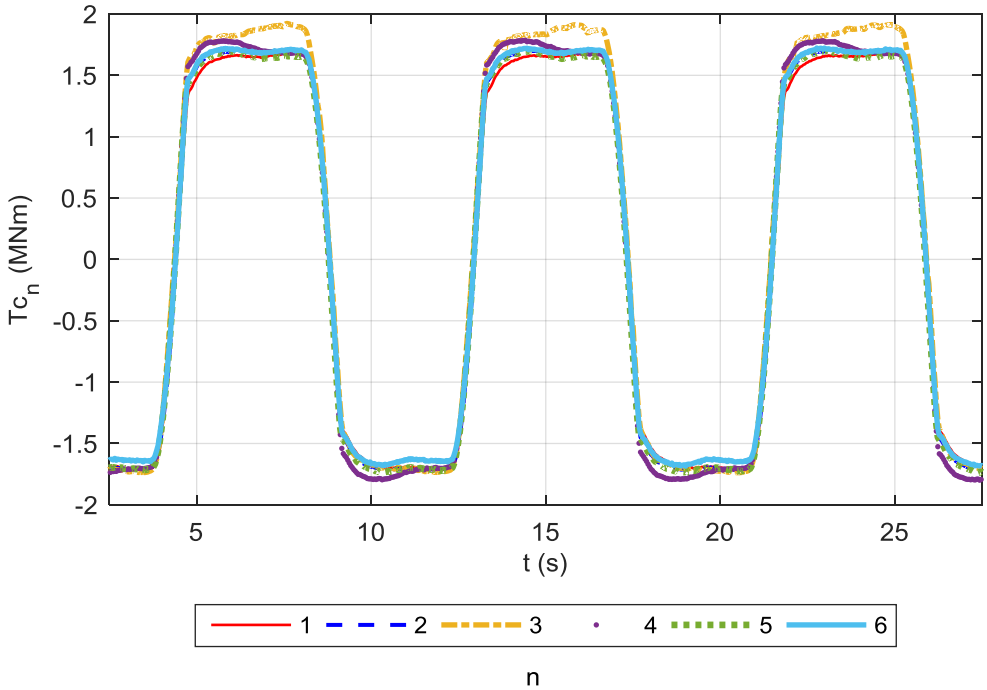

Figure 5. Example of variation in damping torque, Tc_n, with time, t, for six modules (n = 1-6) fixed together in the Rigid Flap configuration.

2.2 Wave Conditions

Regular, head-on waves were used, to generate a fundamental understanding of the Modular Flap. The response of a WEC is generally dependent on the wave period, even for a fairly broad-banded device like a flap-type WEC (Clabby et al., 2012; Whittaker and Folley, 2012). Therefore, the chosen variable for this investigation was the wave period. Eight wave periods were used, approximately evenly spaced between 5.5 s and 13.5 s at full scale. These limits represent the typical range for peak periods at a wave energy site (Babarit et al., 2012). Variation in wave amplitude was not considered as it was not thought to be the most significant parameter relating to power capture. A nominal wave amplitude, of 1 m, at full scale, was selected, with maximum variation of only 2%. The wave direction was not varied either, with all waves being head-on, i.e. with their crests parallel to the hinges of the model. The power-capture of a flap-type WEC is sensitive to direction (Henry, 2008). However, such a device is most likely to be installed in an orientation that matches the mean wave direction

at a site. The head-on case therefore represents the most important condition to first test in. The full range of wave conditions are presented in Table A.1.

2.3 Wave Tank

The QUB Portaferry Wave Tank (Queen's University Belfast, 2016) was selected due to its suitability for shallow water studies, high wave homogeneity (O'Boyle, 2013) and low blockage ratio. A layout of the wave tank, with the model position indicated, is provided in Figure 6. The tank was operated at a depth of 0.463 m at model scale, or 13.9 m at full scale, at the model location.

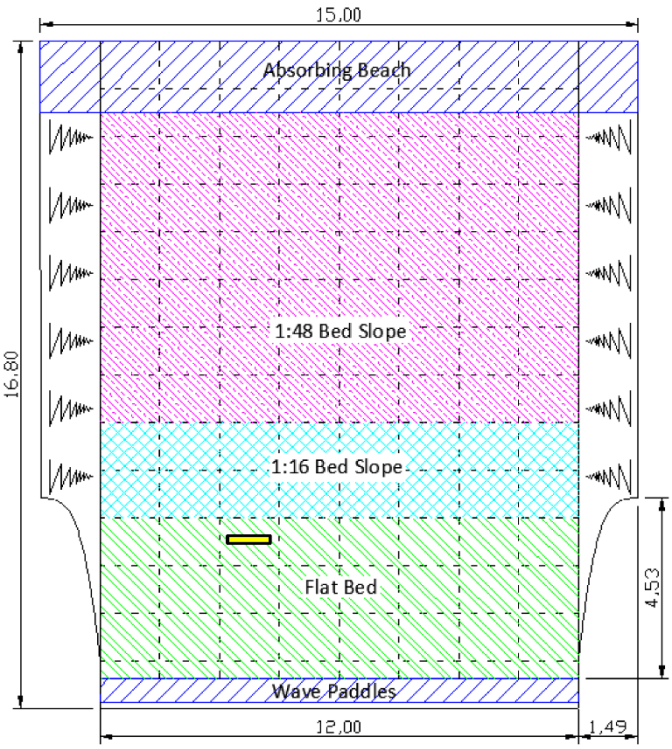

Figure 6. Portaferry Wave Tank layout, to scale, with model scale dimensions in m (O'Boyle, 2013). Model position is indicated by yellow rectangle. Model geometry is approximately to scale.

2.4 Modelling and Analysis Procedures

The aim of the study, as discussed, was to determine the hydrodynamic power-capture achieved by the two devices for a range of wave conditions. In order to achieve this, the total average powers were recorded for a range of damping levels, for each wave condition. The maximum average powers were then determined by fitting a curve through the damping-power pairs, with the peak providing the maximum power. The power-capture was then evaluated using the metric, capture factor. The mean difference in the capture factor values achieved by the two devices, relative to those associated with the Rigid Flap, was then the ultimate metric that was computed. This analysis process started with evaluation of the instantaneous results.

The two instantaneous measurements that were made were damping torque, Tc_n, in MNm, and rotation, θ_n, in radians (rad.). Data were recorded at 128 Hz, at model scale. θ_n was differentiated with respect to time, to find the angular velocity, $\dot{\theta}_n$, in rad/s. These signals were post-processed using a low-pass filter (MathWorks, 2016a), with a cut-off frequency of 5 Hz, at model scale. The instantaneous power, P_n, in kW, was then calculated using Equation 1.

$$P_n = Tc_n\dot{\theta}_n \qquad (1)$$

The instantaneous total power, P_T, was then calculated using Equation 2.

$$P_T = \sum_{n=1}^{M} P_n \qquad (2)$$

Where M is the number of modules, 6.

Each damping level was applied for a duration of 351 s at full scale. The magnitude of each damping level was evaluated as the root-mean-square (RMS) damping torque, $Tc_{n,RMS}$; the equivalent value for the power-capture was the mean power, $\bar{P}_n$. These statistics were generated using Equations 3 and 4, respectively.

$$Tc_{n,RMS} = \sqrt{\frac{\sum_{i=1}^{N} {Tc_{n,i}}^2}{N}} \qquad (3)$$

$$\bar{P}_n = \frac{\sum_{i=1}^{N} P_{n,i}}{N} \qquad (4)$$

Where N is the number of samples in the time series.

The device statistics were the total RMS damping torque, $Tc_{RMS,T}$, and total mean power, $\bar{P}_T$, which were calculated using Equations 5 and 6, respectively.

$$Tc_{RMS,T} = \sum_{n=1}^{M} Tc_{n,RMS} \qquad (5)$$

$$\bar{P}_T = \sum_{n=1}^{M} \bar{P}_n \qquad (6)$$

Another point of interest was how smooth the generated power was. A smoother delivery of power to the electrical grid is less problematic for the network (Molinas et al., 2007). The metric for 'smoothness', S_P, was calculated using Equation 7. A higher S_P value indicates a greater level of smoothing.

$$S_P = \frac{\bar{P}_T}{P_{T,max} - P_{T,min}} \qquad (7)$$

Where $P_{T,max}$ and $P_{T,min}$ are the maximum and minimum values, respectively, of the instantaneous total power, P_T.

The maximum mean power for each wave condition, for each device, $\bar{P}_{T,max}$, was estimated by fitting a quadratic curve to the $Tc_{RMS,T}$, $\bar{P}_T$ pairs and finding the peak. The x-axis value of this peak corresponded to the optimum damping level. An example power curve is provided in Figure 7.

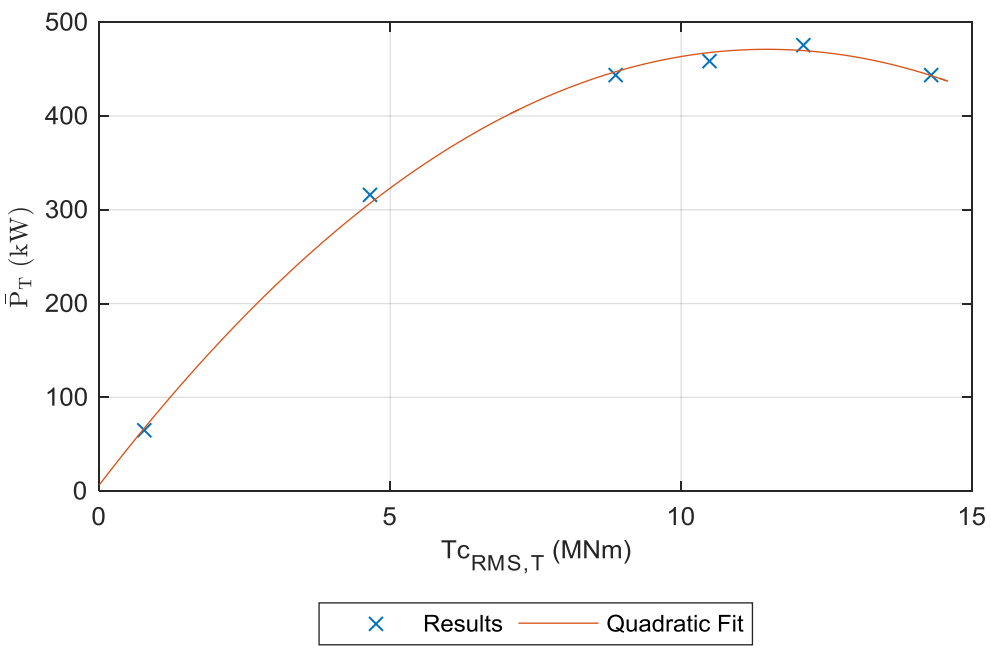

Figure 7. Example of power curve, showing total mean power, $\bar{P}_T$, against total RMS damping torque, $Tc_{RMS,T}$, with quadratic curve fit.

The capture factor, *CF*, is a useful measure of the efficiency of a device (Folley et al., 2007). *CF* is the ratio of generated power, in this case $\bar{P}_{T,max}$, to incident power and was calculated using Equation 8.

$$CF = \frac{\bar{P}_T}{P_{inc}\cos(A)W} \quad (8)$$

Where, P_{inc} is the incident power per metre of crest, in kW/m; A is the installation angle, 0, in rad.; W is the device width, 33.3, in m. P_{inc} was calculated for each wave condition, using standard formulae, provided in (United States Naval Academy, n.d.). The results are presented in Table A.1.

The relative differences in the *CF* values achieved by the two devices, $\Delta CF'$, were then computed using Equation 9.

$$\Delta CF' = \frac{CF_{Mod} - CF_{Rig}}{CF_{Rig}} \quad (9)$$

Where CF_{Mod} and CF_{Rig} are the *CF* values achieved by the Modular and Rigid Flaps, respectively.

The mean relative difference in the *CF* values, $\overline{\Delta CF'}$, was then computed using Equation 10.

$$\overline{\Delta CF'} = \frac{\sum_{j=1}^{P} \Delta CF_j'}{P} \quad (10)$$

Where *P* is the number of wave conditions, 8, and, for the *j*th wave condition, $\Delta CF_j'$ is the relative difference in *CF* values and $CF_{j,Rig}$ is the *CF* value achieved by the Rigid Flap.

2.5 Uncertainty Analysis

An uncertainty analysis was completed to ascertain the usability of the results for statistical significance of the conclusions that were drawn. This section contains some background information, discussion of the uncertainty sources and a description of the calculation method for the dominant source. All calculation methods are provided in Appendix B.

Uncertainties arise from random or systematic errors (Coleman and Steele, 2009), for example due to temperature variation or calibration of sensors, respectively. The outcome of an uncertainty analysis is an estimation of a range, +/- U_X, around the best measurement of a result, X_{best}. It is believed that the true value, X_{true}, lies within this range, to a certain degree of confidence (Coleman and Steele, 2009; Lamont-Kane et al, 2013). In this study, the 95% confidence limit was used, which is standard for engineering applications (Coleman and Steele, 2009). The aim of the uncertainty analysis in this paper was to estimate U_X for the mean relative differences in *CF* between the two devices, $\overline{\Delta CF'}$, as defined in Equation 10, $U_{\overline{\Delta CF'}}$. Only those sources of uncertainty which were deemed significant were considered. These are listed below, with the category of the source provided in brackets:

1. Torque sensor calibration slopes (systematic)
2. Rotation sensor calibration accuracy (systematic)
3. Variation of wave conditions and model behaviour (random)
4. Model orientation (systematic)

The dominant source of uncertainties was number 2, the ‘rotation sensor calibration accuracy’. The reason that this was included was that systematic uncertainties in the rotation signals were noticed. These were made apparent when the modules were fixed together as the Rigid Flap. The measurements of rotation and angular velocity should have been the same for this configuration. However, it was noticed that there were appreciable consistent differences, with an example shown in Figure 8. This issue was thought to have arisen due to the way in which the sensors were calibrated. The sensors were calibrated simultaneously by first fixing the modules together with an aluminium bar. For practical reasons, this was conducted outside of the wave tank. The modules were then installed in the wave tank and fixed together with PVC sheets to form the Rigid Flap. The deviations in velocity may have therefore resulted from the slight differences in constraint, between that supplied by the bar and the PVC sheets.

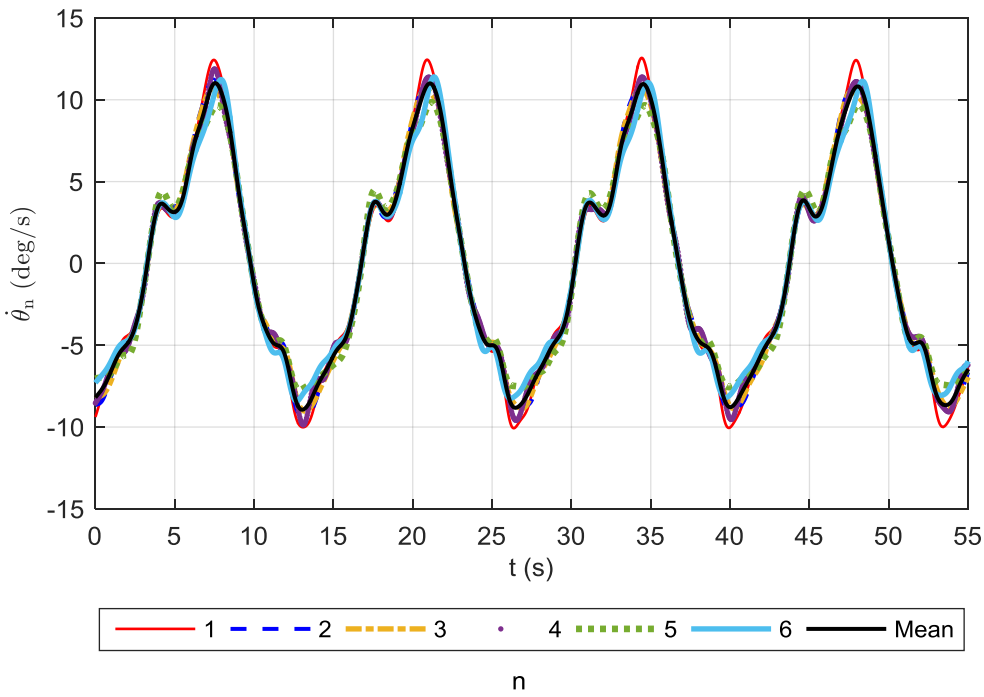

Figure 8. Example of variation in angular velocity, $\dot{\theta}_n$, with time, t, for six modules (n = 1-6), fixed together in the Rigid Flap configuration, and the mean values.

The differences shown in Figure 8 were present across the testing range. This resulted in consistent over or under-estimation of the power produced by each module.

The systematic uncertainties associated with the module velocities were quantified using different, but similar, approaches for the Rigid and Modular Flaps. For the Rigid Flap, direct comparison to the instantaneous mean of the module velocities was used, which was deemed the most accurate method. For the Modular Flap though, as a result of the hydrodynamics, there were natural differences in the velocities of the modules. This meant that comparison to the instantaneous mean velocity could not be used and therefore a different method was applied. If the velocity signals were first approximated as sinusoidal traces, the differences manifested themselves as consistent deviations in their peak spectral amplitudes. The peak amplitudes were found using a Fast Fourier Transform (FFT) (MathWorks, 2016b). The sensor for module 1, for example, consistently had a peak velocity amplitude of approximately 3 deg/s, at model scale, greater than the mean of the peak amplitudes for a particular wave condition. The mean deviation in peak velocity amplitude, for each module, was then used to generate sinusoidal traces of systematic uncertainties in the module velocities.

An example time-series of contributions to systematic uncertainty on the module power is shown in Figure 9. Note that the relative magnitude of the total systematic uncertainties shown in this particular example were comparatively low. However, this example illustrates the dominance of the velocity component.

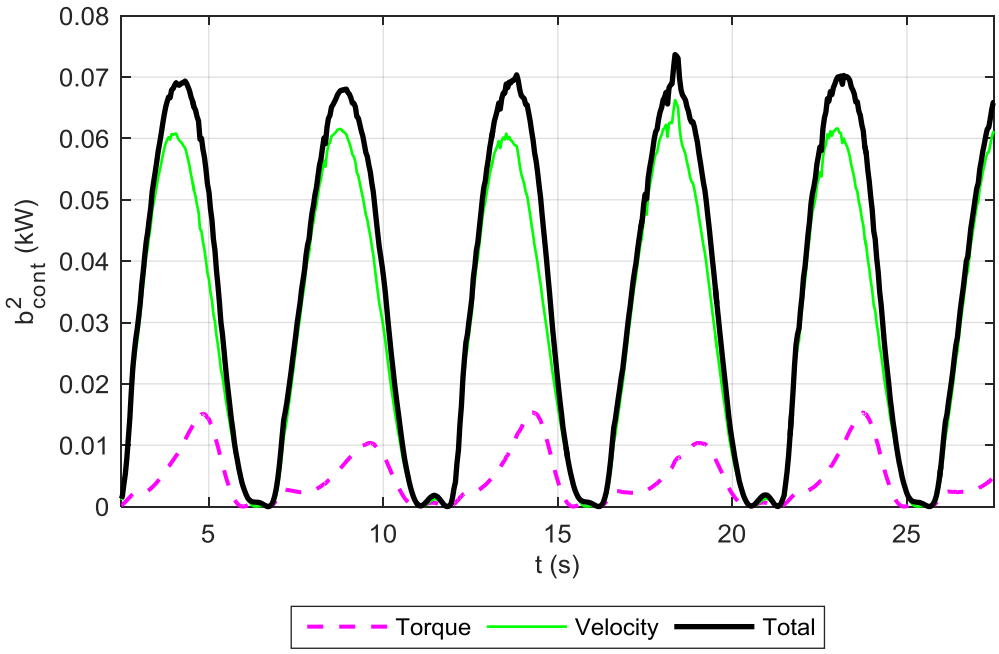

Source

Figure 9. Example plot of variation in squared contributions to systematic uncertainties on module power, b^2_{cont}, with time, *t*, for a single module. b^2_{cont} values were calculated as the squared products of the systematic uncertainty on velocity and damping torque (and vice versa). Please refer to Equation B.4 for further clarification. This example was for the Modular Flap.

The systematic contribution to the combined uncertainty on the total mean power for each damping level was significantly higher than the random contribution. Using the same case shown in Figure 9 as a typical example to demonstrate this, the systematic and random contributions were 97% and 3%, respectively. Please refer to Equation B.8 for clarification on how this was calculated. The combined uncertainty on the maximum total mean power for each wave condition was then the dominant contribution to the uncertainty on the capture factors, *CF*. Using the same example again, the relative expanded uncertainties on the maximum total mean power and the installation angle were 4.4% and 0.8%, respectively. When added in quadrature, it can be seen that the former contribution is dominant. This therefore shows that the systematic uncertainty in the module velocity measurements was the most influential source.

The resulting expanded uncertainties on the *CF* values were 0.02-0.04 (4-8% relative) for the Modular Flap and 0.03-0.06 (6-10% relative) for the Rigid Flap. However, because the devices used the same instrumentation, most of the uncertainties were correlated. This resulted in the absolute expanded uncertainties on the differences between the *CF* values being smaller than the absolute expanded uncertainties on the individual *CF* values. This meant that the experimental system was adequate for showing statistical significance in the mean relative differences in *CF* between the two devices, $\overline{\Delta CF'}$.

3. Results

This section presents the key results from the study. First shown are results for the individual modules, with the model configured as the Modular Flap, followed by those for the whole devices. Within each sub-section, compared first are the power time-series. Inspection of these allows one to gauge their relative magnitudes and phases. This is followed by presentation of mean power results.

3.1 Modular Flap Modules

Figure 10 shows an example of power time-series for modules 1-3, which occupied one side of the model. Also shown are time-series of damping torques and velocities, to allow further understanding of the results.

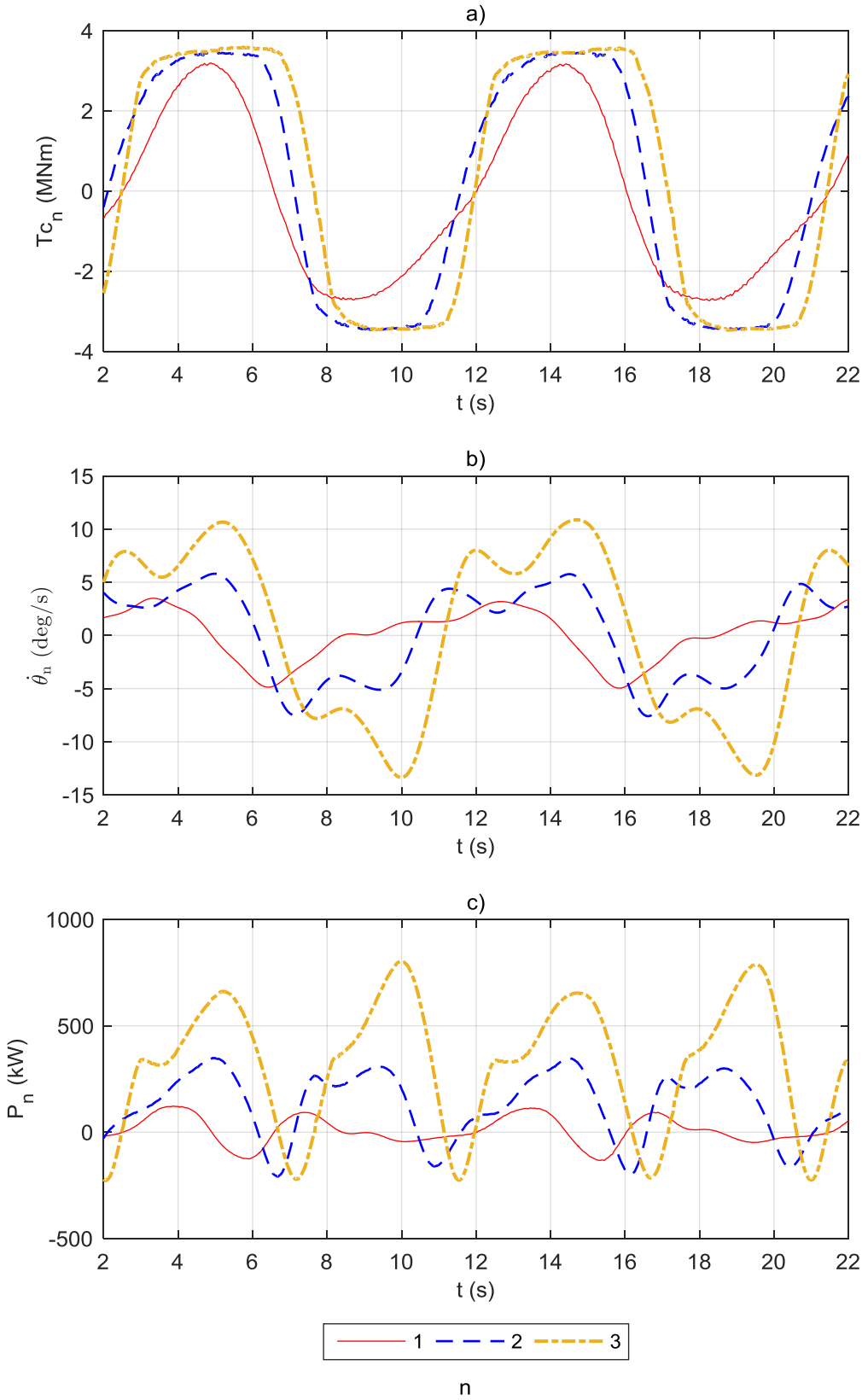

Figure 10. Example of variation of individual module damping torques, Tc_n, (a), velocities, $\dot{\theta}_n$, (b) and powers, P_n, (c) for modules 1, 2 and 3, with time, t.

Firstly, subplot c) of Figure 10 shows that there was a short period of each oscillation where the power was negative. This is thought to have resulted from a spring effect in the dampers when the modules changed direction. This will have injected some torque into the system. For this short period, the damper acted like a motor. The negative power values were included in the calculation of mean power. It is likely though that the effect on the mean power values will have been small. This is because the effect of the negative power phase will likely have been cancelled out by an increase in the positive power due to an increased velocity.

There were also double-peaks present in the velocity and power signals. This may have been due to waves radiated by each flap module interacting with adjacent units. The difference in magnitudes in the maximum values of power for alternate strokes, especially prominent for module 3, were likely due to asymmetry in the surge forces.

The key features of Figure 10**Error! Reference source not found.** though are the differences in magnitudes and phases of the signals. Subplot a) of Figure 10 shows that the damping torque applied to the outer module (n = 1) was approximately sinusoidal in shape. This suggests that the damping torque was greater than the wave excitation torque. This resulted in the module velocities and powers being virtually 0, as shown in subplots b and c, respectively. Moving towards the centre modules, the damping torque signals bared greater resemblance to Coulomb damping profiles. The magnitudes of the velocities and powers also increased towards the centre of the device.

The phase differences in the signals shown in Figure 10 will have been caused by diffracted and radiated waves meeting the different modules at different points in time. The signals for symmetrical pairs, for example modules 3 and 4, were generally in phase. For adjacent modules on one half of the device though, phase differences were present. The greatest difference was between the outer and centre modules, for example numbers 1 and 3. From Figure 10, differences of approximately 1/3 of the wave cycle were present in the velocity and power signals. Across the range of wave periods, there were phase differences in the velocities and powers, though no distinct relationship was shown. This means that the device was displaying similar behaviour to the out-of-phase motions shown by closely-spaced flap units in works such as Adamo and Mei (2005).

The instantaneous values were then averaged to find the mean module powers. The results, for the modules paired about the centre of the device, are compared in Figure 11 across the range of wave periods.

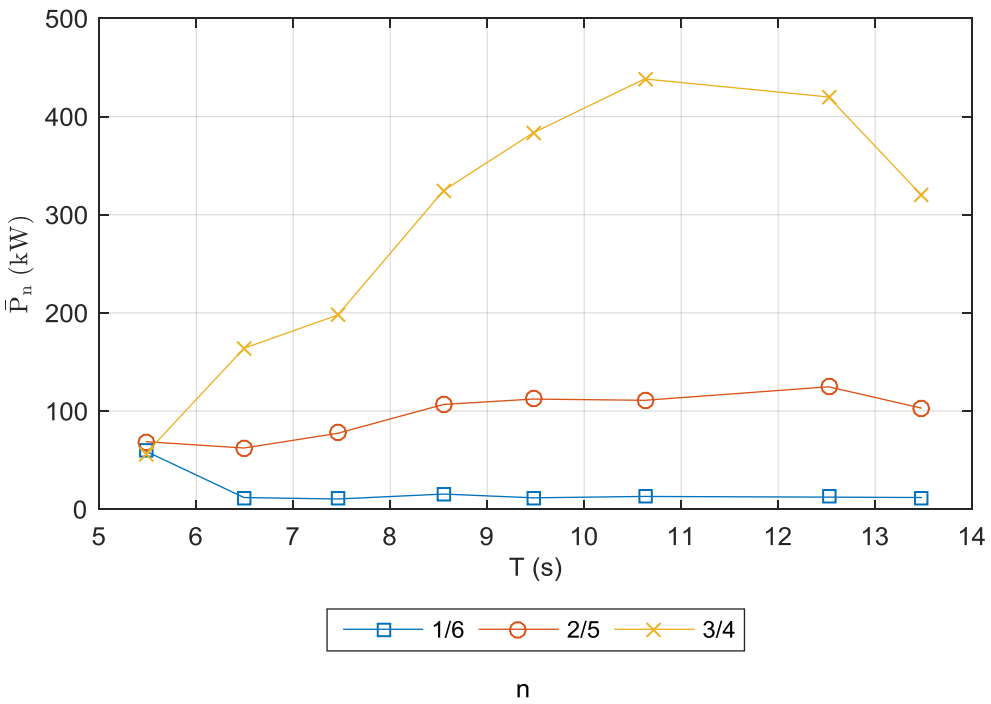

Figure 11. Average mean powers per module for symmetrical pairs of modules, $\bar{P}_n$, against wave period, *T*. The values are from tests that corresponded to the optimum recorded damping level.

Figure 11 shows that the mean powers generally increased towards the centre of the device, with the outer most modules generating least power and the inner most modules generating most. This agrees with the findings by Sarkar et al. (2016). Comparing the mean powers of each set of pairs to the total power produce by the device, the middle modules (3/4) produced 72% of the total power, the inner modules (2/5) 24% and the outer modules (1/6) only 5%. It is likely that this was due to wave excitation torques being greater there, as shown in Sarkar et al. (2016).

As also indicated in Figure 11, the variation of mean module powers changed with wave period. The coefficient of variation was used for comparison. Variation was lowest, at 10 %, for the shortest periods, and highest for the longer periods, maximising at 119% for a period of 10.6 s.

3.2 Devices

It is interesting to assess how the phase differences in the individual instantaneous module powers, shown in Figure 10c, affected the total power produced. The same example as used in Figure 10 was employed to explore this, in Figure 12. Shown for comparison are also the equivalent results for the Rigid Flap.

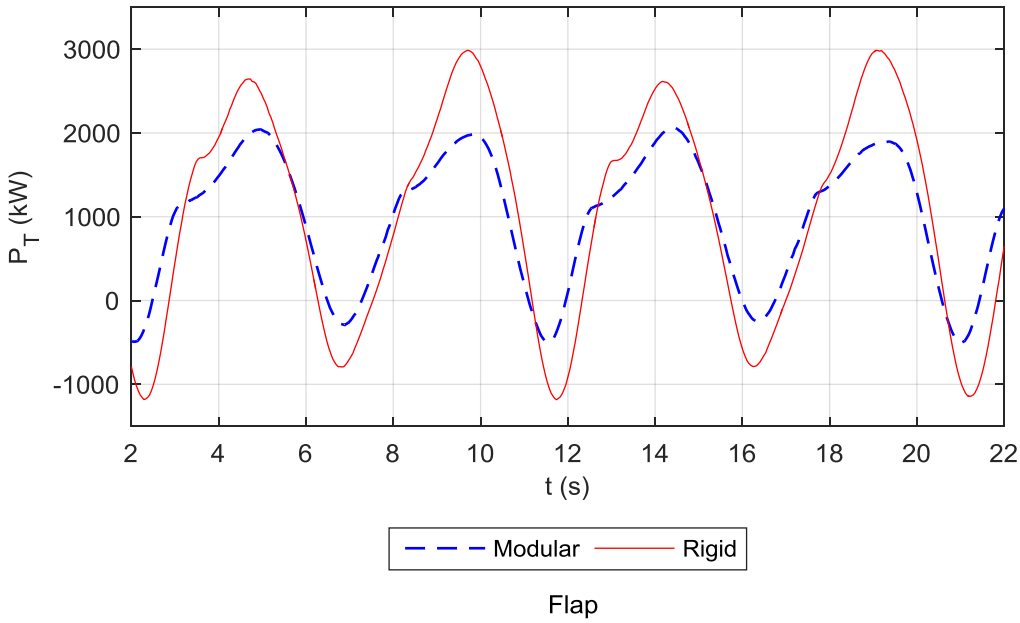

Figure 12. Variation of total power, P_T, with time, t, for Modular and Rigid Flaps. Both devices had the same total damping torque level applied to them. Note that the time has been adjusted so that the time-series approximately overlay.

Figure 12 shows that the total power signal for the Modular Flap, when compared to the individual module powers in Figure 10c, did not have the same relative magnitude of oscillations. While phase differences were shown in the module power values, the total power signal also combined into a single oscillation.

The mean values of the power signals shown in Figure 12 were 1020 kW for the Modular Flap and 1110 kW for the Rigid Flap. The ranges of the powers were 2,600 kW and 4,350 kW, respectively. From these values, the smoothness metric, S_P, was calculated as 0.39 and 0.26, respectively. This indicates a higher level of smoothness for the power generated by the Modular Flap. The S_P values were then calculated for all of the total power time-series that

corresponded to the optimum recorded damping levels. The mean values were 0.38 and 0.29, respectively. This indicates that, using this metric, the total power produced by the Modular Flap was, on average, 28% more smooth. This is likely due to the out-of-phase power production by the individual modules, indicated in Figure 10c.

Presented now are comparisons of the capture factors achieved by the two devices across the range of wave periods. Also computed were the expanded combined uncertainties on the capture factors, defined in Equation B.12, which are depicted as error bars. The results are shown in Figure 13.

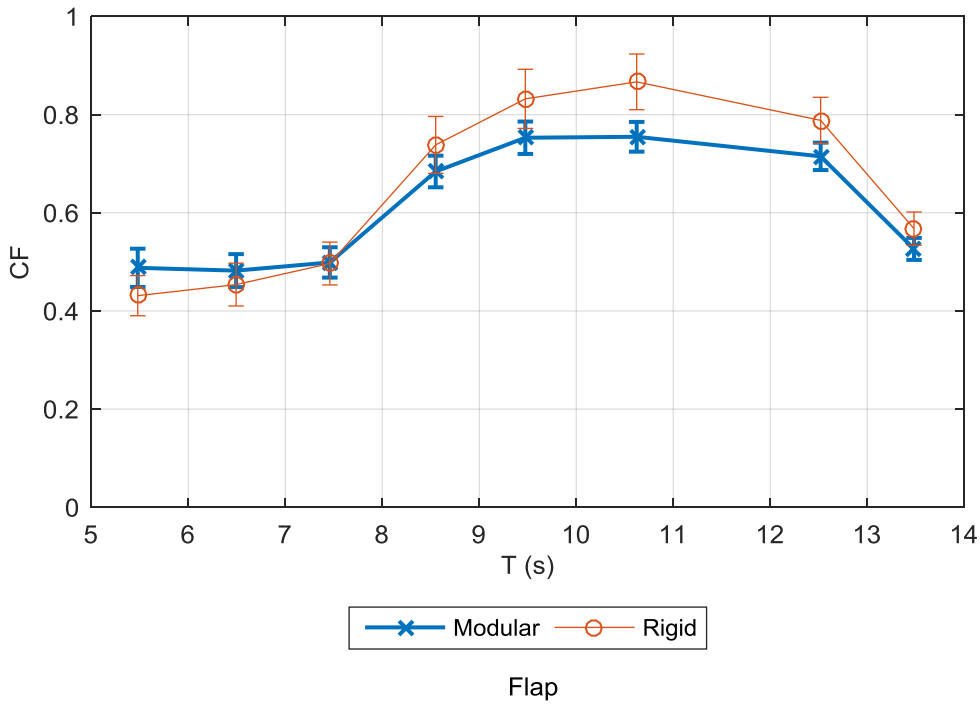

Figure 13. Capture factors, *CF*, with associated expanded combined uncertainties, against wave period, *T*, for the Modular and Rigid Flaps.

Figure 13 shows that both devices achieved relatively high capture factors across the range of wave periods, indicating a broad bandwidth. Though not well defined, both devices peaked at around a period of 10.6 s, with a capture factor of approximately 0.8. Figure 13 also indicates that there was variation in the relative differences in the capture factors achieved by the two devices. Figure 14 shows this in more detail by presenting the computed values for each wave

period.

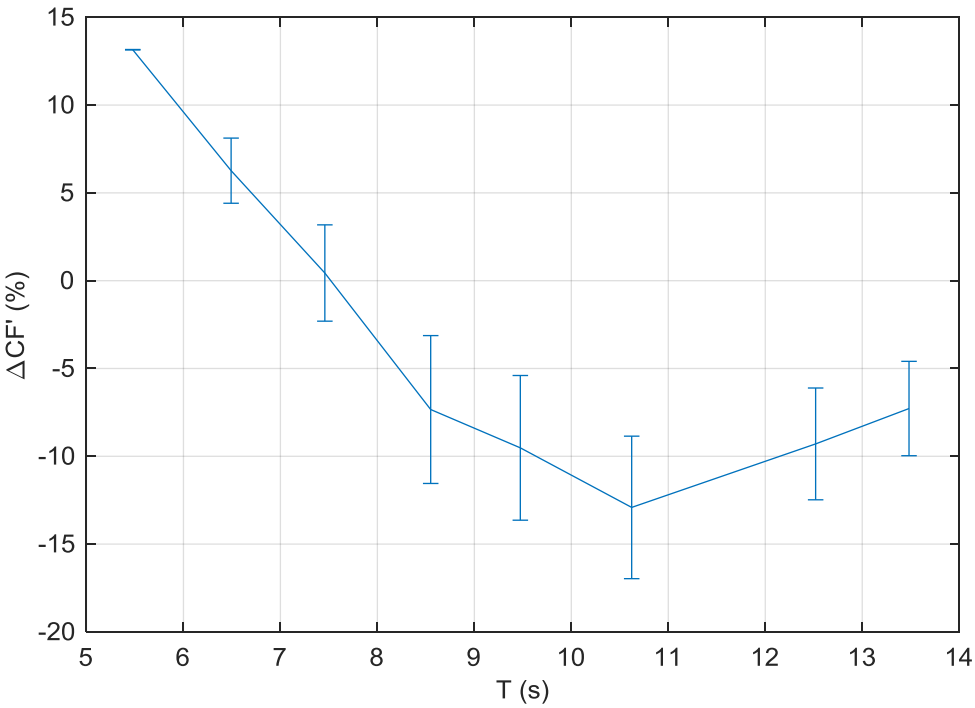

Figure 14. Relative differences in the capture factors, *CF*, achieved by the Modular and Rigid Flaps, *ΔCF'*, with associated expanded combined uncertainties, against wave period, *T*.

Figure 14 shows that there was generally an inverse relationship between the relative differences in capture factor and the wave periods. For the lower wave periods, the Modular Flap outperformed the Rigid Flap, by up to 13%. This may have been due to a near-excitation of a natural mode of the system, such as shown for a similar system in (Adamo and Mei, 2005). For the higher periods though, the Rigid Flap outperformed the Modular Flap by up to 13%. This may have resulted, indirectly, from greater module velocities at the higher wave periods. Due to the higher total surface areas of the sides of the devices, the total shear stresses will have likely been greater for the Modular Flap at these periods. This will therefore have resulted in greater power losses, providing some explanation for the reduced capture factors. The inverse relationship may have also been connected with the variation of the magnitudes of the module rotations. The peak rotation amplitudes were computed, using an FFT, for the tests that corresponded to the optimum recorded damping level. The coefficients of variation, the generic formula for which is defined in Equation B.6, of the amplitudes were then evaluated. Figure 15 shows the relationship between the relative differences in capture factor and these coefficients of variation.

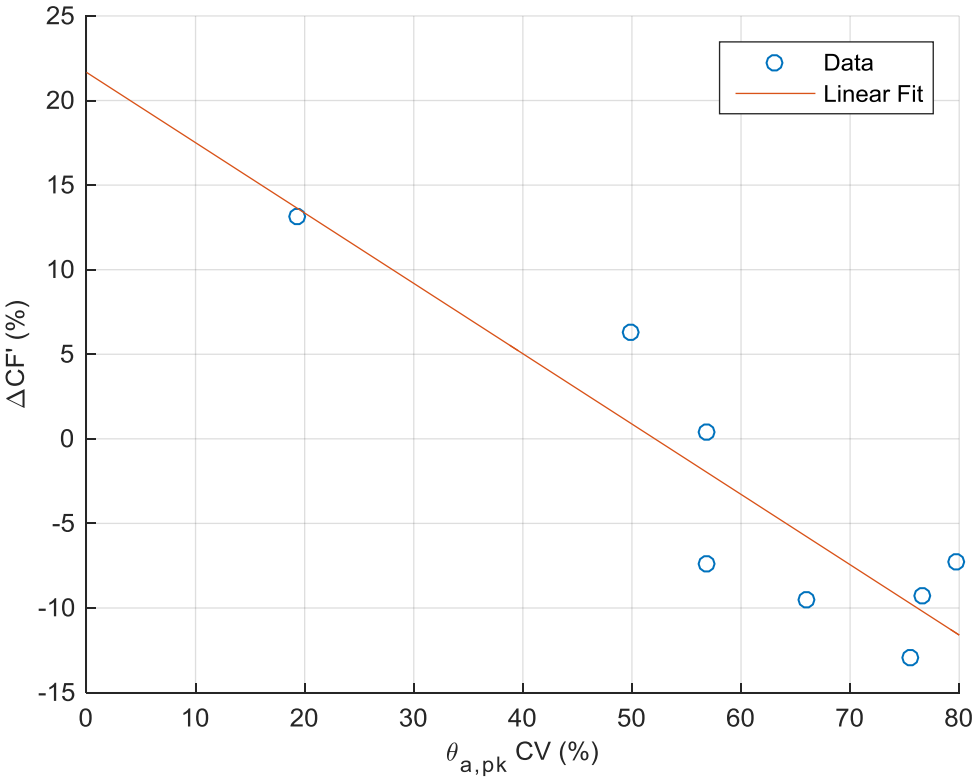

Figure 15. Relative difference in capture factors, *ΔCF'*, against coefficient of variation of peak module rotation amplitudes, $\theta_{a,pk}$ *CV*, for all wave periods. The values are from tests that corresponded to the optimum recorded damping level.

The relationship shown in Figure 15 suggests that there was an inverse correlation between the relative power production and the level of variation in the module rotation amplitudes. This suggests that, with opening up of larger gaps between the modules, water leakage occurs through the gaps, resulting in reduced power production. This suggests that greater power production is achieved by minimising the level of variation of the rotation of the modules. This could be realised by applying different damping levels to each module. The effects of damping strategy on the power-capture of the Modular Flap is an area for further work.

As discussed earlier, the ultimate aim of the study was to compare the power-capture of the Modular Flap to the Rigid Flap for a range of wave conditions. The mean value of the relative differences in the capture factor across the wave periods, shown in Figure 14, was therefore recorded. This was -3.3%, with an expanded combined uncertainty of +/- 2.9%. This shows that there was a statistically significant, but small, reduction in efficiency when comparing the Modular Flap to the Rigid Flap. This was likely due to a combination of increased total shear

stress on the device and small amounts of water leakage through the gaps between the modules.

4.

Discussion

This section provides some reflection on the results, placing them in the wider context. For the Modular Flap, it was shown that there was no significant reduction in power-capture, compared to the Rigid Flap. This was for the case where damping was equal across the modules and, therefore, some degree of validation is also provided for the work by Sarkar et al. (2016). If damping were allowed to vary, as was the case in Sarkar et al. (2016), then greater power production may have been achievable. Nevertheless, the Rigid Flap concept has high conversion efficiency (Babarit, 2015; Babarit et al., 2012). The Modular Flap has advantages, such as reduced parasitic foundation loads (Wilkinson et al., 2014), the possibility of less expensive installation, and, shown in this study, smoother power generation. These benefits can therefore be exploited without significantly compromising one of the flap-type WEC's greatest advantages, its efficiency.

For the Modular Flap, the low rotation amplitudes and power production of the outer modules, especially at longer wave periods, suggests that they were serving the purpose of funnelling the incident wave into the inner modules. For sites characterised by these conditions, it may in fact therefore be most economical to have inexpensive structures, without PTOs, in place of the outer modules.

The results that have been presented here have been for regular, head-on waves. In the real ocean though, waves are irregular. There is also some level of directionality, both in terms of the mean direction and spreading, even in nearshore sites (Herbers et al, 1999). The broad-banded response shown, in Figure 13, though, means that the trends should be similar, for irregular waves, to those shown in regular waves. For directional waves though, it is expected that the Modular Flap would outperform the Rigid Flap, due to the independent operation of the modules.

5. Conclusions

This paper has presented a power-capture assessment of a modular flap-type WEC, referred to here as the 'Modular Flap'. The device was made up of six modules, with a total width, at full-scale, of 33 m. Comparisons were made to a single equivalent unit, named the 'Rigid Flap'. The assessment was carried out with 30th scale physical modelling in a wave tank. The waves that were used were head-on and regular, with the period varied and the amplitude held constant. The simplest damping strategy was employed, which was to damp each module equally.

The power produced by the individual flap modules was very different, with power increasing significantly towards the centre. On average, the central pair of modules produced 72% of the total power, the inner modules 24% and the outer modules only 5%. Phase differences were also shown between the powers produced by the modules. These are thought to have caused a smoothing effect in the total instantaneous power. Using the ratio of the mean to the range as a metric, the Modular Flap produced power that was, on average, 28% more smooth.

On average, the power-capture of the Modular Flap was 3.3% lower than the Rigid Flap. This difference had an expanded combined uncertainty of +/- 2.9%. This shows that there was a small, but statistically significant reduction in power for the Modular Flap. The high conversion efficiency of the flap-type WEC and the range of techno-economic advantages mean though that the Modular Flap is a promising concept.

Further work will evaluate the effects of the use of irregular and directional waves. The potential benefits of employing different damping control strategies will also be investigated. Optimisation of the modular concept, for example in terms of geometry, will also be carried out. This could investigate the effects of parameters such as the size of modules, the total device width and the spacing between the modules.

6.

Acknowledgements

Thank you to the technicians at QUB, for design guidance and model fabrication, and to the QUB Marine Research Group, for support during the experimental campaign and writing of this paper. This work was supported by the Energy Technologies Institute (ETI) and the RCUK Energy Programme for the Industrial Doctoral Centre for Offshore Renewable Energy (grant number EP/J500847/1). Thank you also to the former sponsor of this research, Aquamarine Power Ltd, and, now, QUB for financial support and the latter for provision of experimental testing facilities.

7.

References

Abadie, 2016. Numerical Study of Wave Interaction with a Modular Oscillating Wave Surge Converter.

Adamo and Mei, 2005. Linear response of Venice storm gates to incident waves. Proc. R. Soc. A Math. Phys. Eng. Sci. 461, 1711–1734. doi:10.1098/rspa.2004.1432

Aquamarine Power Ltd, 2011. Projects: Oyster 800 project, Orkney [WWW Document]. URL http://www.aquamarinepower.com/projects/oyster-800-project-orkney.aspx (accessed 7.19.16).

Aquamarine Power Ltd, 2009. Oyster generates £1m for Orkney economy [WWW Document]. URL http://www.aquamarinepower.com/news/oyster-generates-%C2%A31m-for-orkney-economy.aspx (accessed 7.18.16).

AW-Energy, 2012. WaveRoller Concept [WWW Document]. URL http://aw-energy.com/about-waveroller/waveroller-concept (accessed 7.18.16).

Babarit, 2015. A database of capture width ratio of wave energy converters. Renew. Energy 80, 610–628. doi:10.1016/j.renene.2015.02.049

Babarit et al., 2012. Numerical benchmarking study of a selection of wave energy converters. Renew. Energy 41, 44–63. doi:10.1016/j.renene.2011.10.002

Clabby et al., 2012. The Effect of the Spectral Distribution of Wave Energy on the Performance of a Bottom Hinged Flap Type Wave Energy Converter. Rio de Janeiro.

Coleman and Steele, 2009. Experimentation, Validation, and Uncertainty Analysis for Engineers. John Wiley & Sons.

Folley et al., 2007. The design of small seabed-mounted bottom-hinged wave energy converters, in: Proceedings of the 7th European Wave and Tidal Energy Conference.

Henry, 2008. The hydrodynamics of small seabed mounted bottom hinged wave energy converters in shallow water. Queen's University Belfast.

Henry et al., 2010. Advances in the Design of the Oyster Wave Energy Converter, in: Royal Institution of Naval Architect's Marine and Offshore Renewable Energy Conference. Royal Institution of Naval Architect's Marine and Offshore Renewable Energy Conference.

Herbers et al, 1999. Directional spreading of waves in the nearshore zone. J. Geophys. Res. 104, 7683–7693. doi:10.1029/1998JC900092

ITTC, 2014a. ITTC – Recommended Procedures - General guideline for uncertainty analysis in resistance tests. 7.5-02-02-02 (Revision 02).

ITTC, 2014b. ITTC – Recommended Procedures Uncertainty analysis instrumentation calibration. 7.5-01-03-01 (Revision 01).

Lamont-Kane et al, 2013. Investigating Uncertainties in Physical Testing of Wave Energy Converter Arrays, in: Proceedings of 10th European Wave and Tidal Energy Conference.

MathWorks, 2016a. idealfilter [WWW Document]. URL http://uk.mathworks.com/help/matlab/ref/timeseries.idealfilter.html (accessed 9.3.16).

MathWorks, 2016b. fft [WWW Document]. URL http://uk.mathworks.com/help/matlab/ref/fft.html?requestedDomain=www.mathworks.com (accessed 7.11.16).

Mei et al., 1994. Subharmonic resonance of proposed storm gates for Venice Lagoon, in: Proceedings: Mathematical and Physical Sciences. doi:10.1098/rspa.1983.0054

Molinas et al., 2007. Power Smoothing by Aggregation of Wave Energy Converters for Minimizing Electrical Energy Storage Requirements, in: Proceedings of the 7th European Wave and Tidal Energy Conference. doi:10.1016/j.tree.2005.11.022

National Instruments, 2016. LabVIEW System Design Software [WWW Document]. URL http://www.ni.com/labview/ (accessed 7.11.16).

O'Boyle, 2013. Wave Fields around Wave Energy Converter Arrays. Queen's University Belfast.

Queen's University Belfast, 2016. Portaferry Wave Tank [WWW Document]. URL http://www.qub.ac.uk/research-centres/cerc/Facilities/MarineFacilities/PortaferryWaveTank/ (accessed 7.8.16).

Renzi et al., 2014. Wave-power absorption from a finite array of oscillating wave surge converters. Renew. Energy 63, 55–68. doi:10.1016/j.renene.2013.08.046

Sammarco et al., 2013. Flap gate farm: From Venice lagoon defense to resonating wave energy production. Part 1: Natural modes. Appl. Ocean Res. 43, 206–213. doi:10.1016/j.apor.2013.10.001

Sarkar et al., 2016. The modular concept of the Oscillating Wave Surge Converter. Renew. Energy 85, 484–497. doi:10.1016/j.renene.2015.06.012

United States Naval Academy, n.d. EN475 - Ocean Engineering Mechanics - Equation Sheet 1: Linear Wave Properties.

van 't Hoff, 2009. Hydrodynamic Modelling of the Oscillating Wave Surge Converter. Queen's Univ. Belfast.

Whittaker and Folley, 2012. Nearshore oscillating wave surge converters and the development of Oyster. Philos. Trans. A. Math. Phys. Eng. Sci. 370, 345–64. doi:10.1098/rsta.2011.0152

Wilkinson et al., 2015. Modelling the performance of a modular flap-type wave energy converter, in: Proceedings of the 11th European Wave and Tidal Energy Conference.

Wilkinson et al., 2014. Wave Loads on the Foundation of a Bottom-Hinged Modular Flap Structure, in: Offshore Renewable Energy ORE.

Appendix A - Wave Conditions

Wave Identifier	Model-Scale			Full-Scale		
	Measured Wave Amplitude, *a* (m)	Wave Period, *T* (s)	Incident Wave Power, P_{inc} (W/m)	Measured Wave Amplitude, *a* (m)	Wave Period, *T* (s)	Incident Wave Power, P_{inc} (kW/m)
1	0.033	2.5	9.82	0.99	13.5	48.4
2	0.033	2.3	9.44	0.99	12.5	46.5
3	0.033	1.9	9.04	1.00	10.6	44.6
4	0.033	1.7	8.18	0.98	9.5	40.3
5	0.034	1.6	7.97	1.01	8.5	39.3
6	0.033	1.4	7.01	1.00	7.5	34.6
7	0.033	1.2	5.95	1.00	6.5	29.3
8	0.033	1.0	4.72	1.00	5.5	23.3

Table A.1. List of wave conditions that were used.

Appendix B - Uncertainty Analysis Calculations

This section provides details on how the uncertainties on the results were calculated. The ultimate aim of the analysis was to calculate the expanded uncertainty on the mean relative difference in capture factors achieved by the Modular and Rigid Flaps, $U_{\overline{\Delta CF'}}$. Formulae were used and adapted from Coleman and Steele (2009) and publications by the ITTC (2014a, 2014b). The uncertainties in the measured variables were propagated to the results through the use of the Taylor Series Method (TSM), a standard technique (Coleman and Steele, 2009).

The uncertainty analysis was started at the instantaneous level, instead of using the mean values, as carried out in ITTC (2014a), because of the periodic nature of the test data. Only the

systematic uncertainties were considered at the instantaneous level. This was because it was assumed that the random instantaneous fluctuations in the signals would have a negligible impact on the generated statistics, e.g. the mean module powers.

The systematic uncertainties on the instantaneous damping torque signals, b_{Tc_n}, in MNm, were calculated using Equation B.1.

$$b_{Tc_n} = V_n b_{m_{Tc,n}} \qquad \text{(B.1)}$$

Where, for the *n*th torque sensor, V_n is the instantaneous recorded voltage, in V, and $b_{m_{Tc,n}}$ is the systematic uncertainty on the calibration slope, in MNm/V. The $b_{m_{Tc,n}}$ values were quantified using the method provided in ITTC (2014b). The absolute and relative $b_{m_{Tc,n}}$ values are provided in Table C.1.

The systematic uncertainties on the instantaneous module angular velocity, $b_{\dot{\theta}_n}$, in rad./s, were calculated using Equations B.2 and B.3 for the Rigid Flap and Modular Flap, respectively.

$$b_{\dot{\theta}_n} = \dot{\theta}_n - \bar{\dot{\theta}} \qquad \text{(B.2)}$$

Where, $\bar{\dot{\theta}}$ is the instantaneous mean of the module angular velocity, $\dot{\theta}_n$, values with the model configured as the Rigid Flap.

$$b_{\dot{\theta}_n} = \bar{\Delta}\dot{\theta}_{a,n}\cos(2\pi f_{pk} t + \varphi_{pk}) \qquad \text{(B.3)}$$

Where, $\bar{\Delta}\dot{\theta}_{a,n}$ is the mean of the differences between the peak amplitudes of the module angular velocities and the mean of the values, across the range of wave conditions, in rad./s, f_{pk} is the peak frequency of the incident wave, in Hz, *t* is the time, in s, and φ_{pk} is the phase of the incident wave for f_{pk}, in rad.

The instantaneous systematic uncertainties on the module powers, b_{P_n}, in kW, were calculated using a sum of squares approach as given by Equation B.4. Note that the uncertainties on module damping torques, Tc_n, and angular velocities, $\dot{\theta}_n$, were assumed to be uncorrelated.

$$b_{P_n} = \sqrt{{Tc_n}^2 {b_{\dot{\theta}_n}}^2 + {\dot{\theta}_n}^2 {b_{Tc_n}}^2} \qquad \text{(B.4)}$$

The relative systematic uncertainties on the mean module powers were significantly higher than the equivalent values for the RMS module damping torques. Therefore, only the systematic uncertainties on the mean module powers, $b_{\bar{P}_n}$, are considered here and were calculated with Equation B.5. This method allowed consideration of the correlation between the values throughout the time-series.

$$b_{\bar{P}_n} = \frac{\sum_{i=1}^{N} b_{P_{n,i}}}{N} \qquad \text{(B.5)}$$

Where *N* is the number of samples in the time series.

The random uncertainties on the power-capture were evaluated using a set of repeat tests for each device. The test was conducted by leaving the waves running for five test durations and keeping the damping levels the same. A single, mid-range wave condition, of period 8.5 s and nominal amplitude 1.01 m was used. The level of variation was then assumed constant across the range of wave conditions. This variation was measured using the coefficient of variation (*CV*), which presents the standard deviation of a dataset as a fraction of the mean. The generic formula for *CV* is provided in Equation B.6.

$$CV_X = \frac{s_X}{\bar{X}} \quad \text{(B.6)}$$

Where, s_X is the standard deviation of the sample of repeat measurements of variable *X* and $\bar{X}$ is the mean of the repeat *X* measurements.

The random uncertainties for the total mean power-capture, $s_{\bar{P}_T}$, were calculated using Equation B.7.

$$s_{\bar{P}_T} = \frac{CV_{\bar{P}_T}\bar{P}_T}{\sqrt{N}} \qquad \text{(B.7)}$$

Where, $CV_{\bar{P}_T}$ is the *CV* value for the total mean power capture and N is the number of repeats, 5. At only 0.7% for the Modular Flap and 0.3% for the Rigid Flap, the CV values were low enough to not contribute significantly to the standard combined uncertainties on the total mean power capture.

$b_{\bar{P}_n}$ and $s_{\bar{P}_T}$ were then used to find the standard combined uncertainties on the total mean power capture, $u_{\bar{P}_T}$, using Equation B.8.

$$u_{\bar{P}_T} = \sqrt{\left(\sum_{n=1}^{M} b_{\bar{P}_n}{}^2\right) + s_{\bar{P}_T}{}^2} \qquad \text{(B.8)}$$

The standard combined uncertainty on the maximum total mean power, $u_{\bar{P}_{T,max}}$ was then estimated. This involved calculating $u_{\bar{P}_T}$ for each damping level, defined by the total RMS damping torque, $Tc_{RMS,T}$. The $Tc_{RMS,T}$-$u_{\bar{P}_T}$ pairs were then plot, with a quadratic curve subsequently fit through the data. The $u_{\bar{P}_{T,max}}$ value was then the value on the curve that corresponded to the optimum damping level, i.e. the one that resulted in maximum power generation.

The expanded combined uncertainties on the capture factors, U_{CF}, were then calculated. The $u_{\bar{P}_{T,max}}$ values were first considered as systematic uncertainties, as shown in Equation B.9.

$$b_{\bar{P}_{T,max}} = u_{\bar{P}_{T,max}} \quad \text{(B.9)}$$

The standard combined uncertainty on the capture factors, u_{CF}, was then calculated using Equation B.10.

$$u_{CF} = \sqrt{\frac{b_{\bar{P}_{T,max}}{}^2 + b_{\cos(A)}{}^2}{P_{inc}{}^2 W^2}} \quad \text{(B.10)}$$

Where, $b_{\cos(A)}$ is the systematic uncertainty on the cosine of the installation angle. $b_{\cos(A)}$ was calculated using Equation B.11.

$$b_{\cos(A)} = 1 - \cos(b_A) \qquad \text{(B.11)}$$

Where, b_A, is the systematic uncertainty on the installation angle, which was estimated to be, quite conservatively, 5 deg. U_{CF} was then calculated using Equation B.12.

$$U_{CF} = k_p u_{CF} \qquad \text{(B.12)}$$

Where, k_p is the coverage factor, 2, for a 95% confidence level (ITTC, 2014a).

The standard combined uncertainty on the differences in capture factors achieved by the two devices, $u_{\Delta CF}$, were then calculated using Equation B.13.

$$u_{\Delta CF} = \sqrt{\frac{{b_{\bar{P}_{T,max,Rig}}}^2 + {\bar{P}_{T,max,Rig}}^2 {b_{\cos(A)}}^2 + {b_{\bar{P}_{T,max,Mod}}}^2 + {\bar{P}_{T,max,Mod}}^2 {b_{\cos(A)}}^2 - 2 b_{\bar{P}_{T,max,Rig}} b_{\bar{P}_{T,max,Mod}}}{{P_{inc}}^2 W^2}}$$

(B.13)

Where terms with 'Rig' or 'Mod' in their subscripts referring to values associated with the Rigid and Modular Flaps, respectively.

The standard combined uncertainties on the relative differences of the capture factors, $u_{\Delta CF}{}'$, were then calculated using Equation B.14.

$$u'_{\Delta CF} = \sqrt{\frac{{u_{\Delta CF}}^2}{{CF_{Rig}}^2} + \frac{{\Delta CF}^2}{{CF_{Rig}}^4} {u_{CF,Rig}}^2 - 2 \frac{\Delta CF}{{CF_{Rig}}^3} u_{\Delta CF} u_{CF,Rig}} \qquad \text{(B.14)}$$

The expanded combined uncertainties on the relative differences of the capture factors, $U_{\Delta CF}{}'$, were then calculated using Equation B.15.

$$U'_{\Delta CF} = k_p u'_{\Delta CF} \qquad \text{(B.15)}$$

The mean expanded combined uncertainty on the relative differences of the capture factors, $U_{\overline{\Delta CF'}}$, was then calculated using Equation B.16.

$$U_{\overline{\Delta CF'}} = \frac{\sum_{j=1}^{P} U'_{\Delta CF\,j}}{P} \qquad \text{(B.16)}$$

Where, *P* is the number of wave conditions, 8, and $U'_{\Delta CF\,j}$ is the expanded combined uncertainty on the relative difference of the capture factors for the *j*th wave condition.

Appendix C - Torque Sensor Calibration Slope Uncertainties

Torque Sensor No., *n*	**Calibration Slope Uncertainty (Model Scale) $b_{m_{Tc,n}}$ (Nm/V)**	**Calibration Slope Uncertainty (Full Scale) $b_{m_{Tc,n}}$ (MNm/V)**	**Relative Calibration Slope Uncertainty, $b_{m_{Tc,n}}$' (%)**
1	0.0014	0.0011	-0.15

2	0.0004	0.0003	-0.04
3	0.0019	0.0015	-0.21
4	0.0009	0.0007	-0.10
5	0.0010	0.0008	-0.11
6	0.0037	0.0030	-0.42

Table C.1. Absolute and relative torque sensor calibration slope uncertainties.